Projection onto Convex Sets (POCS) Method for Photoacoustic Tomography with a Non Negative Constraint

S. M. Akramus Salehin, Shaochun Huang and Thushara D. Abhayapala

Abstract— Photoacoustic imaging is a biomedical imaging modality capable of early cancer detection. In this paper, we proposed a novel iterative Projections Onto Convex Sets (POCS) method for improving photoacoustic reconstruction. This method aims to obtain a non negative pressure distribution satisfying the measured signals. This POCS method is performed in the Fourier Bessel space avoiding matrix inversions in the projections, speeding up projections and is capable of handling the large data sets present in photoacoustic imaging. The numerical experiments performed showed that improved reconstruction was obtained with a few iterations together with the recovery of some lost information.

Index Terms— Convex projections, photoacoustic tomography, thermoacoustic, Fourier Bessel series, POCS

I. INTRODUCTION

Photoacoustic imaging uses a laser pulse to thermally excite the sample under test. This thermal excitation causes acoustic waves that are detected by sensors. The rate of absorption of optical energy from the laser pulse is dependent on the type of tissue. Photoacoustic imaging can be used for early cancer detection, blood vessel imaging, small animal imaging and has several other biomedical imaging uses [1].

The Projection Onto Convex Sets (POCS) method recovers a function in the intersection of convex sets. This method is applied for image recovery and uses a sequence of alternating projections onto these sets. This method is popular for biomedical imaging with applications in MRI [2], in computed tomography [3] and several other image restoration applications (see [3] and the references therein).

In normal photoacoustic inversion, the reconstruction must satisfy both the measured data as well as the pressure distribution being non negative. In previous reconstruction methods reviewed in [1], the values less than zero were simply set to zero. We propose an iterative, POCS method that reconstructs a pressure distribution satisfying both the non negativity constraint and the measured data. The projections are done in the Fourier Bessel space avoiding matrix inversions, providing fast projections and is capable of dealing with the large data sets present in photoacoustic imaging. We show that the POCS methods results in better quality reconstruction with the recovery of some lost information. In a previous paper, the authors have shown how incorporating a total variation (TV) minimization approach better reconstructions are possible [4]. In this paper, the proposed POCS method does not require prior knowledge that the image is piecewise constant as is required by the TV minimization method.

The contributions of this paper are as follows. We show that significant improvements in the reconstructed image can be obtained by incorporating a non negative constraint on the image which must also satisfy the measured data. Further, an efficient POCS based method in the Fourier Bessel domain is proposed to find an image satisfying both the non-negativity constraint and the measured signals. This method has the advantage of utilizing fast Fourier Bessel transforms and not requiring the computation of the inverse of a large matrix. Hence, is suitable for photoacoustic reconstruction where we have large datasets.

This paper is organized as follows. Section 2 discusses photoacoustic inversion. Section 3 describes the POCS method in the Fourier Bessel space, the projection operators, the numerical algorithm to implement the POCS method and its extension to 3D photoacoustic inversion. Section 4 discusses the numerical experiments performed and Section 5 provides a summary of the main ideas presented in this paper.

II. PHOTOACOUSTIC THEORY

The photoacoustic inversion problem assuming constant speed of acoustic waves c can be formulated mathematically in the frequency domain as

$$p(\boldsymbol{r}_s, k) = -ikc \int_V p_0(\boldsymbol{r}) G(k; \boldsymbol{r}_s, \boldsymbol{r}) \, \mathrm{d}\boldsymbol{r} \qquad (1)$$

where $p(\boldsymbol{r}_s, k)$ is the measured pressure at sensor position $\boldsymbol{r}_s$, $\int_V (\cdot) \mathrm{d}\boldsymbol{r}$ is the integration over a volume, k is the wavenumber equal to $2\pi f/c$ with f the frequency, $p_0(\boldsymbol{r})$ is the initial pressure distribution and $G(\cdot)$ is the 3D Green's function.

The 2D photoacoustic inverse problem is formulated as

$$p(\boldsymbol{r}_s, k) = -ikc \int_S p_0(\boldsymbol{r}) G_{2D}(k; \boldsymbol{r}_s, \boldsymbol{r}) \, \mathrm{d}\boldsymbol{r} \qquad (2)$$

where $\int_S (\cdot) \mathrm{d}\boldsymbol{r}$ is integration over a surface and $G_{2D}(\cdot)$ is the 2D Green's function. The 2D inverse problem occurs when the pressure distribution $p_0(\boldsymbol{r})$ varies over two dimensions with point sensors or when the z-averaged pressure distribution is reconstructed using integrating line sensors. A detailed description and derivation of the 2D photoacoustic inverse problem is provided in [5].

III. PROPOSED POCS METHOD FOR PHOTOACOUSTIC INVERSION

We consider a 2D source distribution $p_0(\boldsymbol{r})$ contained within a 2D ball $B(r_0)$ with bounding radius r_0 and the

sensors are placed in a circle of radius r_s greater than the bounding radius. The source distribution is expanded with a 2D Fourier Bessel series expansion

$$p_0(\boldsymbol{r}) = \sum_{m=-\infty}^{\infty} \sum_{\ell=1}^{\infty} \beta_{m\ell} \Psi_{m\ell} \qquad (3)$$

where $\beta_{m\ell}$ are complex, Fourier Bessel coefficients and the basis functions are

$$\Psi_{m\ell} \triangleq \frac{1}{\sqrt{\pi}} \frac{1}{r_0 J_{m+1}(z_{m\ell})} J_m\left(\frac{z_{m\ell}}{r_0} r\right) e^{im\phi}. \qquad (4)$$

where $J_m(\cdot)$ is the Bessel function of mode m, $z_{m\ell}$ is the ℓth root of $J_m(\cdot)$ and ℓ is the zero index.

The 2D Fourier Bessel series are a complete orthonormal expansion for the Hilbert space of square integrable functions on the 2D ball $L^2(B(r_0))$ with the inner product

$$\langle p_0(\boldsymbol{r}), f(\boldsymbol{r}) \rangle \triangleq \int_0^{2\pi} \int_0^{r_0} p_0(\boldsymbol{r}) \overline{f(\boldsymbol{r})} r \, dr \, d\phi. \qquad (5)$$

where $\overline{(\cdot)}$ is the complex conjugate operator.

The discrete version of this inner product replaces the integration with sums by applying numerical integration methods such as the trapezoidal method.

The method introduced in [6] calculates the Fourier Bessel coefficients $\beta_{m\ell}$ by taking the spatial Fourier transform of the aperture at frequencies corresponding to the Bessel zeros i.e., at $k = z_{m\ell}/r_0$ and then dividing by a suitable weight.

A. Projections from Measurements

In practice, measurements are taken for a finite bandwidth with k_l the lower and k_u the upper frequency limit. From this bandwidth, only a finite set of Fourier Bessel coefficients can be calculated and these belong the set $\Lambda = \{m, \ell | k_l \leq z_{m\ell}/r_0 \leq k_u\}$. Therefore, the measurements are satisfied by a set of source distributions which satisfy the following condition

$$\langle p_0(\boldsymbol{r}), \Psi_{m\ell} \rangle = \widetilde{\beta}_{m\ell} \text{ for } \forall\{m, \ell\} \in \Lambda \qquad (6)$$

where $\widetilde{\beta}_{m\ell}$ are the calculated Fourier Bessel coefficients. The set of source distributions satisfying this constraint will be denoted by set A.

B. Projection Operators

We define an index limiting operator as follows.

Definition 1 (Index Limiting Operator): The index limiting operator for the Hilbert space $L^2(B(r_0))$ is a truncated Fourier Bessel transform

$$(\mathcal{B}_\Lambda p_0)(\boldsymbol{r}) = \sum_{\{m,\ell\} \in \Lambda} \langle p_0(\boldsymbol{r}), \Psi_{m\ell} \rangle \Psi_{m\ell} \qquad (7)$$

and can be thought of as a filter on $B(r_0)$.

The complement of the index limiting operator is

$$(\mathcal{B}_{\Lambda^C} p_0)(\boldsymbol{r}) = p_0(\boldsymbol{r}) - (\mathcal{B}_\Lambda p_0)(\boldsymbol{r}) \qquad (8)$$

where Λ^C is the complement of set Λ. From these definitions, the projection to preserve the calculated coefficients $\widetilde{\beta}_{m\ell}$ is derived as

$$(\mathscr{P}_A p_0)(\boldsymbol{r}) = (\mathcal{B}_{\Lambda^C} p_0)(\boldsymbol{r}) + \sum_{\{m,\ell\} \in \Lambda} \widetilde{\beta}_{m\ell} \Psi_{m\ell}. \qquad (9)$$

For any source distribution $p_0(\boldsymbol{r})$, this projection adds the contributions from the calculated coefficients to the source distribution from which the contribution of these available basis functions has been removed beforehand.

In normal POCS method, calculation of an inverse matrix is required. In photoacoustics where we have large data set, this becomes computationally expensive. In the Fourier Bessel space, the projections provided by the measured data are converted to projections of the pressure distribution onto a set of orthonormal basis functions and so avoids calculating the inverse of a matrix. Further, the projections and synthesis onto the orthonormal Fourier Bessel series can be performed with the Fast Fourier Transform (FFT) and the fast Bessel transforms [7]. This speeds up the calculation of this projection and speed of reconstruction is an important factor in photoacoustic inversion.

The pressure distribution is also non negative i.e., $p_0(\boldsymbol{r}) \geq 0$. The set distributions satisfying this non negativity convex constraint is denoted by set B and the projection operator $\mathscr{P}_B$ simply sets all negative values in $p_0(\boldsymbol{r})$ to zero.

C. Numerical Algorithm

The initial distribution is obtained by

$$\widehat{p_0}^{(0)}(\boldsymbol{r}) = \sum_{\{m,\ell\} \in \Lambda} = \widetilde{\beta}_{m\ell} \Psi_{m\ell} \qquad (10)$$

and uses the available coefficients in the measured data $\widetilde{\beta}_{m\ell}$.

A new source distribution is obtained by projecting onto B. This removes the index limiting property of the first pressure distribution. Then a projection to preserve the calculated coefficients $\widetilde{\beta}_{m\ell}$ are performed. This process is repeated iteratively

$$\begin{aligned} \widetilde{p}_0^{(\kappa)}(\boldsymbol{r}) &= (\mathscr{P}_B \widehat{p}_0^{(\kappa)})(\boldsymbol{r}) \\ \widehat{p}_0^{(\kappa+1)}(\boldsymbol{r}) &= (\mathscr{P}_A \widehat{p}_0^{(\kappa)})(\boldsymbol{r}) \\ \kappa &= 0, 1, 2, \dots \end{aligned} \qquad (11)$$

where κ is the iteration index.

A sequence of pressure distributions are generated that eventually converges to $p_0^\star(\boldsymbol{r}) \in A \cap B$ and is shown by Fig. 1. In the implementation, we utilized the discrete version of the inner product.

D. Proof Convergence

We adapt the convergence proof for the normal POCS method provided in [8] to show that our proposed method converges. In the POCS method, each projection brings the initial pressure distribution $p_0^{(\kappa)}(\boldsymbol{r})$ closer to $p_0^\star(\boldsymbol{r})$, and we
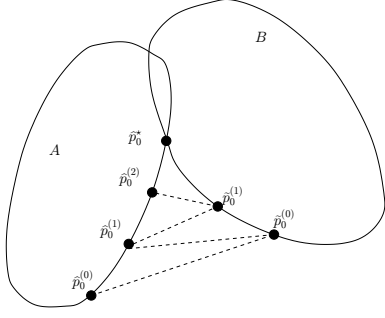
Fig. 1: Our POCS method iteratively projects onto the sets A and B.

can show this by

$$\|\widehat{p}_0^{(\kappa)}(\boldsymbol{r}) - p_0^\star(\boldsymbol{r})\|^2 = \|\widehat{p}_0^{(\kappa)}(\boldsymbol{r}) - \widetilde{p}_0^{(\kappa)}(\boldsymbol{r}) + \widetilde{p}_0^{(\kappa)}(\boldsymbol{r}) - p_0^\star(\boldsymbol{r})\|^2$$
$$= \|\widehat{p}_0^{(\kappa)}(\boldsymbol{r}) - \widetilde{p}_0^{(\kappa)}(\boldsymbol{r})\|^2 + \|\widetilde{p}_0^{(\kappa)}(\boldsymbol{r}) - p_0^\star(\boldsymbol{r})\|^2$$
$$+ 2(\widehat{p}_0^{(\kappa)}(\boldsymbol{r}) - \widetilde{p}_0^{(\kappa)}(\boldsymbol{r}))^T(\widetilde{p}_0^{(\kappa)}(\boldsymbol{r}) - p_0^\star(\boldsymbol{r}))$$
$$\geq \|\widehat{p}_0^{(\kappa)}(\boldsymbol{r}) - \widetilde{p}_0^{(\kappa)}(\boldsymbol{r})\|^2 + \|\widetilde{p}_0^{(\kappa)}(\boldsymbol{r}) - p_0^\star(\boldsymbol{r})\|^2. \tag{12}$$

The last inequality was derived by using a property of the Euclidean projection which satisfies

$$B \subseteq \{\widetilde{p}_0^{(\kappa)}(\boldsymbol{r}) \mid (\widehat{p}_0^{(\kappa)}(\boldsymbol{r}) - \widetilde{p}_0^{(\kappa)}(\boldsymbol{r}))^T(\widetilde{p}_0^{(\kappa)}(\boldsymbol{r}) - p_0^\star(\boldsymbol{r})) \leq 0\} \tag{13}$$

since $\widetilde{p}_0^{(\kappa)}(\boldsymbol{r})$ is the projection of $\widehat{p}_0^{(\kappa)}(\boldsymbol{r})$ onto set B. Rearranging (12), we get

$$\|\widetilde{p}_0^{(\kappa)}(\boldsymbol{r}) - p_0^\star(\boldsymbol{r})\|^2$$
$$\leq \|\widehat{p}_0^{(\kappa)}(\boldsymbol{r}) - p_0^\star(\boldsymbol{r})\|^2 - \|\widehat{p}_0^{(\kappa)}(\boldsymbol{r}) - \widetilde{p}_0^{(\kappa)}(\boldsymbol{r})\|^2. \tag{14}$$

Applying a similar method as that for obtaining (14), we get another inequality

$$\|\widehat{p}_0^{(\kappa+1)}(\boldsymbol{r}) - p_0^\star(\boldsymbol{r})\|^2$$
$$\leq \|\widetilde{p}_0^{(\kappa)}(\boldsymbol{r}) - p_0^\star(\boldsymbol{r})\|^2 - \|\widehat{p}_0^{(\kappa+1)}(\boldsymbol{r}) - \widetilde{p}_0^{(\kappa)}(\boldsymbol{r})\|^2. \tag{15}$$

The inequality (14) shows that $\widetilde{p}_0^{(\kappa)}(\boldsymbol{r})$ is closer to $p_0^\star(\boldsymbol{r})$ than $\widehat{p}_0^{(\kappa)}(\boldsymbol{r})$ and in turn, the inequality (15) shows that $\widehat{p}_0^{(\kappa+1)}(\boldsymbol{r})$ is closer to $p_0^\star(\boldsymbol{r})$ than $\widetilde{p}_0^{(\kappa)}(\boldsymbol{r})$. Hence, the sequence

$$\|\widehat{p}_0^{(0)}(\boldsymbol{r}) - p_0^\star(\boldsymbol{r})\|, \|\widetilde{p}_0^{(0)}(\boldsymbol{r}) - p_0^\star(\boldsymbol{r})\|,$$
$$\|\widehat{p}_0^{(1)}(\boldsymbol{r}) - p_0^\star(\boldsymbol{r})\|, \|\widetilde{p}_0^{(1)}(\boldsymbol{r}) - p_0^\star(\boldsymbol{r})\|, \ldots \tag{16}$$

is decreasing and converges. Since both sequences $\widehat{p}_0^{(\kappa)}(\boldsymbol{r})$ and $\widetilde{p}_0^{(\kappa)}(\boldsymbol{r})$ converge to $p_0^\star(\boldsymbol{r})$, therefore $p_0^\star(\boldsymbol{r}) \in A \cap B$.

In our proof of convergence, we assumed that the intersection of sets A and B is non-empty, but when measurements are contaminated by noise, this assumption may not always be true. In such a case, we need to modify our POCS method to incorporate a stopping criteria to reach a best solution. This is still ongoing work to incorporate such a stopping criteria.

E. Extension to 3D

In this section, we consider a 3D source distribution $p_0(\boldsymbol{r})$ contained within a 3D ball $B^2(r_0)$ using a spherical array of sensors all placed at a radius r_s greater than r_0. This source distribution is in a Hilbert space of square integrable function within the ball i.e., $p_0(\boldsymbol{r}) \in L^2(B^2(r_0))$ with the following inner product

$$\langle p_0(\boldsymbol{r}), f(\boldsymbol{r}) \rangle \triangleq \int_{\Omega \in \mathbb{S}^2} \int_0^{r_0} p_0(\boldsymbol{r})\overline{f(\boldsymbol{r})} \, r\mathrm{d}r \, \mathrm{d}\Omega \tag{17}$$

where the integration over the 2-sphere $\mathbb{S}^2$ is $\int_{\Omega \in \mathbb{S}^2}(\cdot)\mathrm{d}\Omega \triangleq \int_0^{2\pi} \int_0^\pi \sin\theta \, \mathrm{d}\theta\mathrm{d}\phi$, θ is the elevation, ϕ is the azimuth and $\Omega \equiv (\theta, \phi)$.

The spherical Fourier Bessel series

$$\Phi_{nm\ell} \triangleq \frac{\sqrt{2}}{r_0^{3/2} j_n(z_{n\ell})} \, j_n\left(\frac{z_{n\ell}}{r_0}r\right) Y_{nm}(\Omega) \tag{18}$$

forms a complete orthonormal basis function for $L^2(B^2(r_0))$ where $j_n(\cdot)$ are the spherical Bessel functions of order n, $z_{n\ell}$ are the ℓth root of $j_n(\cdot)$ and $Y_{nm}(\cdot)$ are the spherical harmonics. Therefore, the source distribution $p_0(\boldsymbol{r})$ is expanded with this series

$$p_0(\boldsymbol{r}) = \sum_{n=0}^\infty \sum_{m=-n}^n \sum_{\ell=1}^\infty \alpha_{nm\ell}\Phi_{nm\ell} \tag{19}$$

where the spherical Fourier Bessel coefficients are $\alpha_{nm\ell}$.

The method introduced in [9] calculates the spherical Fourier coefficients by applying the spherical Fourier Transform [10] to the aperture at frequencies corresponding to the spherical Bessel zeros i.e., $k = z_{n\ell}/r_0$ and then dividing the result by a suitable weight.

As before, the measurement bandwidth is finite, hence, the set of coefficients that can be recovered belong to the set $\Lambda = \{n, \ell | k_l \leq z_{n\ell}/r_0 \leq k_u\}$. Therefore, the pressure distributions must satisfy the following convex constraint due to the measured data

$$\langle p_0(\boldsymbol{r}), \Phi_{nm\ell} \rangle = \widetilde{\alpha}_{nm\ell} \text{ for } \forall \{n, \ell\} \in \Lambda \tag{20}$$

as well as the non negativity constraint. The projection operators can be defined similar to the 2D case and the numerical POCS method presented in Section III-C can be applied for 3D photoacoustic reconstruction.

IV. NUMERICAL EXPERIMENTS

Numerical experiments were conducted to investigate the improvements in the inversion by applying the proposed POCS method. These numerical experiments were done for the 2D case. However, similar results can be obtained for the 3D case.

The numerical phantom used in the simulations is shown in Fig. 2a. The signals generated by the circular discs were produced according to the formula described in [11], $c = 1500$ m/s which is the speed of sound in biological tissue, $r_0 = r_s = 10$ mm. The recorded pressure signals have a bandwidth from 100 KHz to 1 MHz.
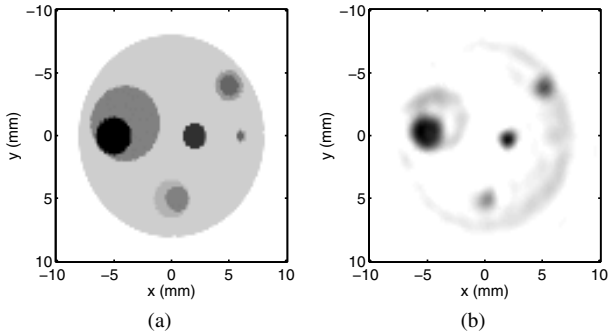
Fig. 2: (a) Numerical phantom composed of several circular discs. (b) First reconstruction of the pressure distribution, i.e. reconstruction obtained from (10).

Noise was added to the generated pressure signals according to

$$\text{SNR} = 10\log_{10}\left(\frac{\int_0^{T_s} |p(\boldsymbol{r}_{ref}, t)|^2 \, dt}{T_s \sigma_n^2}\right) \quad (21)$$

where the reference sensor is the sensor placed at a angular position $\phi = 0$ and T_s is total amount of time for which the signals are recorded. This time T_s was set to $(r_s + r_0)/c$ and 20 dB of noise was added to the generated signals.

In the first inversion shown by Fig. 2b, we observe that large structures are not fully reconstructed since the lower frequency limit is larger than zero. This first inversion is similar to that obtained using any of the previously proposed inversion methods reviewed in [1]. However, the boundaries of these large structures are present in these reconstructions. This is because the low frequency components of the numerical phantom cannot be obtained form these measurements.

The resulting reconstruction by applying POCS method after 10 and 50 iterations are shown in Fig. 3. The POCS method produces images that are significantly better than the first reconstruction. Moreover, some of the lost, low frequency information can be recovered by applying the POCS method.
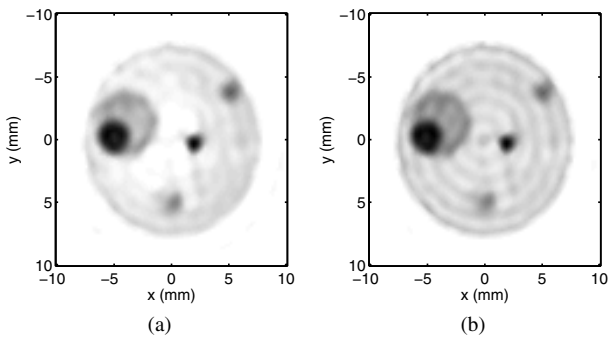

Fig. 3: Resulting reconstruction by applying the proposed POCS method (a) after 10 iterations and (b) after 50 iterations.

After each iteration, the resulting image gets closer to the optimum image and to each of the constraint sets. We also observed that significant improvements occur up to about 10 iterations. Therefore, after a few iterations no significant improvement in image quality is obtained.

In Fig. 3(b), we observe that there are ring artifacts present. This is due to the frequency bandlimit of the recorded acoustic pressure, meaning that only a limited number of Fourier Bessel coefficients $\beta_{m\ell}$ of the initial pressure distribution can be obtained. These ringing artifacts were removed in [4] by applying a Total Variation (TV) constraint to the reconstructed image (initial pressure distribution).

V. CONCLUSIONS

In this paper, we have derived a POCS method for photoacoustic reconstruction which avoids the computation of an inverse of a large matrix by working in the Fourier Bessel space. This also leads to faster projections and an algorithm capable of dealing with the large data sets present in photoacoustic tomography. With a few iterations of the POCS method, significant improvements in reconstruction are obtained together with the recovery of some lost information. POCS method is a popular technique in other biomedical imaging modalities, we expect the POCS method to gain popularity for photoacoustic imaging as well.

REFERENCES

[1] M. Xu and L. V. Wang, "Photoacoustic imaging in biomedicine," *Review of Scientific Instruments*, vol. 77, pp. 041101–1, 2006.

[2] A.A. Samsonov, E.G. Kholmovski, D.L. Parker, and C.R. Johnson, "Pocsense: Pocs-based reconstruction for sensitivity encoded magnetic resonance imaging," *Magnetic resonance in medicine*, vol. 52, no. 6, pp. 1397–1406, 2004.

[3] Y. Censor, W. Chen, P.L. Combettes, R. Davidi, and G.T. Herman, "On the effectiveness of projection methods for convex feasibility problems with linear inequality constraints," *Computational Optimization and Applications*, pp. 1–24, 2011.

[4] S. M. A. Salehin and T. D. Abhayapala, "Constrained total variation minimization for photoacoustic tomography," in *Acoustics, Speech and Signal Processing (ICASSP), 2012 IEEE International Conference on.* IEEE, 2012, pp. 561–564.

[5] S. M. A. Salehin and T. D. Abhayapala, "Frequency domain, photoacoustic tomography with sparse frequency samples," in *Signal Processing Systems (SIPS), 2010 IEEE Workshop on*, oct. 2010, pp. 260 –265.

[6] S. M. A. Salehin and T. D. Abhayapala, "Photoacoustic image reconstruction from a frequency-invariant source localization perspective," in *European Signal Processing Conference (EUSIPCO)*, 2010.

[7] M. O'Neil and V. Rokhlin, "A new class of analysis-based fast transforms," Technical Report YALE/DCS/TR1384, Yale University, 2007.

[8] W. Cheney and A.A. Goldstein, "Proximity maps for convex sets," *Proceedings of the American Mathematical Society*, vol. 10, no. 3, pp. 448–450, 1959.

[9] S. M. A. Salehin and T. D. Abhayapala, "Frequency-radial duality based photoacoustic image reconstruction," *The Journal of the Acoustical Society of America*, vol. 132, pp. 150–161, 2012.

[10] J. R. Driscoll and D. M. Healy, "Computing Fourier transforms and convolutions on the 2-sphere," *Advances in Applied Mathematics*, vol. 15, no. 2, pp. 202–250, 1994.

[11] G. J. Diebold, T. Sun, and M. I. Khan, "Photoacoustic monopole radiation in one, two, and three dimensions," *Physical Review Letters*, vol. 67, no. 24, pp. 3384–3387, Dec 1991.